Observation of a two-mode resonant state in a Bi_{2}Sr_{2}CaCu_{2}O_{8+δ} mesa device for terahertz emission

T. M. Benseman, A. E. Koshelev, V. Vlasko-Vlasov, Y. Hao, U. Welp, W.-K. Kwok, B. Gross, M. Lange, D. Koelle, R. Kleiner, H. Minami, M. Tsujimoto, and K. Kadowaki

Phys. Rev. B **100**, 144503 — Published 7 October 2019

DOI: 10.1103/PhysRevB.100.144503

Observation of a two-mode resonant state in a $Bi_2Sr_2CaCu_2O_{8+\delta}$ mesa device for terahertz emission

T. M. Benseman,[1,2,*] A. E. Koshelev,[2] V. Vlasko-Vlasov,[2] Y. Hao,[2,3] U. Welp,[2,*] W.-K. Kwok,[2] B. Gross,[4] M. Lange,[4] D. Koelle,[4] R. Kleiner,[4] H. Minami,[5] M. Tsujimoto[2,5] and K. Kadowaki[6]

[1]Department of Physics, CUNY Queens College, 6530 Kissena Blvd., Flushing NY 11367

[2] Materials Science Division, Argonne National Laboratory, Lemont IL 60439

[3] Department of Physics, University of Illinois at Chicago, 845 W. Taylor St., Chicago IL 60607

[4] Physikalisches Institut and Center for Collective Quantum Phenomena in LISA$^+$, Universität Tübingen, Auf der Morgenstelle 14, D-72076 Tübingen, Germany

[5] Institute for Materials Science, University of Tsukuba, Ibaraki 305-8753, Japan

[6] Algae Biomass and Energy System (ABES) Research & Development Center, University of Tsukuba, Ibaraki 305-8573, Japan

[*] corresponding authors

Abstract

Using low-temperature scanning laser microscopy (LTSLM), we have studied the cavity resonance behavior of a rectangular $Bi_2Sr_2CaCu_2O_{8+\delta}$ mesa THz device containing $N = 640$ stacked intrinsic Josephson junctions. Our results show that this microscopy technique is an effective means of mapping electromagnetic resonances in this type of device, and we present a detailed analysis of the mechanisms underlying contrast formation in scanning laser microscopy. The LTSLM images reveal that the THz excitation of the stacked junctions contains more than one mode with components along both the long and short axes of the mesa. Thermoluminescent mapping of the same device shows that the mesa temperature is uniform demonstrating that the features seen in LTSLM are electromagnetic in origin, not thermal. Our results also imply that for the purposes of maximizing the THz emission power

from $Bi_2Sr_2CaCu_2O_{8+\delta}$ mesas, it is important to design devices which are capable of being excited in a single, purely transverse mode.

Introduction

Stacked 'intrinsic' Josephson junctions (IJJs) in extremely anisotropic high-temperature superconductors such as $Bi_2Sr_2CaCu_2O_{8+\delta}$ (Bi-2212) provide a promising basis for development of highly compact sources of coherent radiation in the so-called 'terahertz gap' range, [1]. This region of the electromagnetic spectrum spans approximately 0.5 THz to 1.5 THz, and is poorly served by existing solid-state sources, despite being of interest for many applications in science, medicine, security and defense, and high-bandwidth communications technology [2, 3, 4].

Stacked IJJ THz sources operate by DC-to-AC conversion of electrical energy via the AC Josephson effect, whereby a Josephson junction generates an AC current with frequency $f_J = V_{DC}/\Phi_0$, where V_{DC} is the junction DC bias voltage, and Φ_0 is the flux quantum. Generation of far-field radiation requires efficient phase-synchronization of the junctions in the stack, and a number of mechanisms for achieving this have been explored since the discovery of the intrinsic Josephson effect in Bi-2212 [5]. The highest power levels observed have been generated using devices in which the stack is microfabricated in the shape of a resonant cavity that is electromagnetically coupled to the individual IJJs [1, 6, 7]. The cavity-mode frequencies are determined by the spectrum of Josephson plasma waves propagating inside a layered superconductor [8]

$$\omega_p^2(\boldsymbol{k}) \approx \omega_{p0}^2 + \frac{c_0^2\left(k_x^2 + k_y^2\right)}{\varepsilon_c(1 + \lambda_{ab}^2 k_z^2)}, \qquad (1)$$

where c_0 is the speed of light in free space, ε_c is the *c*-axis far-infrared relative dielectric constant of Bi-2212, and λ_{ab} is its *ab*-plane magnetic penetration depth (which depends on temperature). The first term, the Josephson plasma frequency ω_{p0} , is suppressed in the

resistive state. The cavity modes have a transverse magnetic structure with the magnetic field aligned parallel to the CuO_2 planes yielding linearly polarized emitted radiation [7]. The cavity may thus synchronize the IJJs when the stack is biased such that the Josephson frequency matches a resonance mode [6, 7]. Through refinement of this approach, THz emission power levels of up to 0.61 mW [9] and frequencies of up to 2.4 THz [10,11] have been obtained. THz emission has been observed resulting from the cavity modes of round, triangular, [12,13] and pentagonal mesas [14]. However, recently circular polarization has been observed from square mesas with two chamfered corners [15] and from round mesas with broken symmetry [16] indicating more complicated mode structures (see below). In a different approach, Josephson emission at frequencies up to 11 THz has been achieved from small Bi-2212 mesas with lateral sizes of less than 10 μm as detected by a second mesa placed in the near-field [17].

For the purposes of maximizing power output, the most effective shape is a long rectangle. The cavity-mode frequencies are determined by the in-plane mode velocity c_n which, in turn, depends on the *c*-axis wave vector k_z, see Eq. (1). The latter is set by the vertical periodicity and the boundary conditions at the top and bottom. For a junction stack with thickness t containing a large number, $N \gg 1$, of junctions and for boundary conditions that can be expressed as nodes or antinodes, we have $k_z = n\pi/2t$ with n = 0, 1, 2, …, and the mode velocity becomes [18,19]:

$$c_n^2 \approx \frac{c_0^2}{\varepsilon_c[1 + (n\pi\lambda_{ab}/2t)^2]}, \qquad (2)$$

for mode indices $n \ll N/2$. Permitted values for n depend upon the boundary conditions at the top and bottom of the mesa as described further below. As λ_{ab} increases with temperature, the mode velocities for nonzero n decrease with temperature. A junction stack in the form of

a rectangular box supports Fabry-Perot type resonances that approximately correspond to integer numbers of half-periods of the *c*-axis electric field across the width, $w = L_x$, and length, $l = L_y$, of the mesa [12, 20], such that the in-plane electromagnetic wavelengths are given as $\Lambda_{x,y} \approx 2L_{x,y}/m_{x,y}$. The frequency of the ($n$, m_x, m_y)$^{\text{th}}$ cavity mode is expressed as

$$f_{n,\ m_x, m_y} \approx \frac{c_n}{2}\sqrt{\left(\frac{m_x}{w}\right)^2 + \left(\frac{m_y}{l}\right)^2}. \quad (3)$$

Starting from the earliest studies of large rectangular Bi-2212 mesas [7] the frequency of the strongest emission from any given mesa has been found to scale approximately as 1/*w*, indicating that the cavity mode which synchronizes the junctions and which radiates most efficiently has a transverse component, and is indeed typically the (n, 1, 0) mode. This is consistent with the observed (θ, ϕ) angular distribution of the emitted THz radiation [21] in which radiation is most strongly emitted in the direction normal to the long faces of the mesa.

The cavity modes being excited have been probed more directly by low-temperature scanning laser microscopy (LTSLM) [22-26]. In this technique, a focused 680-nm laser beam is modulated at 9 kHz, and rastered across the surface of a current-biased device. Any resulting modulation in the sample voltage can be mapped using a lock-in amplifier, allowing the geometry of the cavity resonances to be studied. Both localized hot spots [23-26] and standing wave-like features [22-24] – most probably corresponding to a cavity resonance – have been observed in previous LTSLM studies. These imaging studies have clearly revealed the longitudinal component of the cavity mode in rectangular mesas. In contrast, experimental evidence for the transverse mode is sparse [27]. This contradicts the commonly observed angle dependence of the THz emission and the approximate 1/*w* scaling of the frequency, which indicate that for most mesas, the cavity modes responsible for THz

emission contain a single half-period across the width of the mesa. This is to say that they are of the form $(n, 1, m_y)$, where m_y is most typically equal to zero [20]. However, in the previous LTLSM work it was not possible to distinguish various possible phenomena that are actually being probed, namely electromagnetic modes or inhomogeneous temperature distributions.

Here, we present LTSLM *and* thermal imaging results on the same BSCCO mesa with width 60 μm and length 360 μm containing 640 IJJs, see Fig. 1. The part of the mesa used in the LTSLM imaging with length 240 μm is covered with a layer of gold with a comparatively small thickness of 30 nm (part I), while the remaining part of the mesa (part II) is covered with a 500 nm thick gold contact. Such nonuniform thickness of the gold contact affects the mode structure inside the mesa, because the mode velocities are different in the two parts. As a consequence, the total length should not fit an integer number of standing-wave periods in the y direction. Nevertheless, we will preserve the standard convention, and will keep the mode notation as (n, m_x, m_y), where the *non-integer* index m_y is defined as the ratio $2l/\Lambda_y$, and Λ_y is the period of the standing wave in part I of the mesa, which can be directly accessed by LTSLM imaging.

We found that the mesa emits most strongly at frequency 396 GHz at a bath temperature of 75 Kelvin. Under these conditions, it generates an LTSLM pattern, which shows roughly five periods along the total length of the mesa, and one clearly resolved period across its width. Note that one full period in the LTSLM pattern correspond to half-period of the cavity electric field, $\Lambda_{x,y}/2$. While this definitively confirms the existence of the transverse mode component, our LTSLM results indicate that the nature of the THz excitation of this mesa must be more complicated than simply a (n, 1, m_y) cavity mode, as the observed mode patterns do not agree with expectations based on an analysis of the different contributions to

the overall observed LTSLM pattern, the details of which are presented in the Appendix. The in-plane and out-of-plane quasiparticle conductivities are perturbed by local heating, as are the in-plane and out-of-plane supercurrent densities, and the penetration depth. Our findings are consistent with the formation of composite modes as have recently been seen in asymmetric mesas [15,16].

Results and Discussion

The mesa studied in this experiment was fabricated on the surface of an optimally-doped Bi-2212 single crystal (T_c = 86.5 K) using optical lithography and argon ion milling, with overall dimensions $60 \times 360 \times 0.992$ μm^3 ($w \times l \times t$). The stack contains N = 640 IJJs. The surface of the mesa was protected from air and water vapor with an evaporated Au film 30 nm thick. In order for the modulated laser beam to be able to significantly thermally perturb the Bi-2212, this Au film must be made comparatively thin. For top electrodes thicker than about 40 nm, most of the power delivered by the 680 nm laser will be reflected, and there will be very little resulting modulation in the mesa voltage. Current is supplied via a sputtered 500 nm Au thin film lead, which only covers one end of the mesa (see schematics in Fig. 1 and the photo in Fig. 2). The base crystal underneath the mesa was only 100 nm thick and was mounted on a copper substrate using tin-lead solder, resulting in very effective heat removal from the device. In contrast to previous work on BSCCO mesas patterned on thick base crystals, self-heating was negligible in the samples described here under the biasing conditions needed for THz emission, and LTSLM measurements could be performed which probed the cavity resonance alone.

When operating the mesa as a THz source, the bias current is initially swept up until all the IJJs are driven into the resistive state, after which the current is swept down until mesa

voltages appropriate for THz generation are reached. Detectable THz emission occurs at a range of cryogenic bath temperatures spanning from approximately 63 K to 77 K. Figure 2(c) shows scanning laser results at T_{bath} = 75 K, at which temperature THz emission from the device was maximized. Curves for the mesa voltage and THz emission signal as a function of bias current are plotted in Figure 2(b). The 'wiggles' in the mesa current occurring between 0.55 V and 0.60 V mark the excess current that drives the cavity resonances and the emission. The scanning laser images clearly reveal a standing wave-like structure, whose greatest amplitude coincides closely with conditions for maximum intensity of THz emission. Indeed, as Figure 2 shows, the standing wave is only present when detectable far-field THz radiation is being generated. The standing wave shows the same qualitative pattern over the entire range of bath temperatures for which THz emission occurs. (Images for T_{bath} = 65 K are plotted in the Appendix.) It should be noted, however, that the THz emission power, scanning laser images, and thermoluminescent images were measured in three different cryostats. There could consequently be small systematic shifts of the current-voltage characteristics between these three systems owing to minor differences in calibrations of the temperature or bias current. Current-voltage curves measured in these three cryostats are compared in the Appendix. These show that over the range of currents at which THz radiation was generated, no systematic shift of the current-voltage curves between the cryostats could be observed at a level greater than 100 microamperes.

The longitudinal structure of the wave varies depending on the bias voltage. The oscillations cannot be observed all the way to the current-lead end of the mesa, since the thick Au current lead reflects the laser beam and prevents it from thermally coupling to the device itself. Nevertheless, vestiges of a wave pattern are visible alongside the thick current contact. In the longitudinal direction and at low bias current we observe three periods in the LTSLM patterns to the left of the current contact and two beneath it, while at higher current there

appear four (or more) periods to the left of the contact whereas the number under the contact does not seem to change, see also the longitudinal profiles shown in Figure 3(a). A maximum of the LTLSM intensity appears to be pinned to the edge of the current contact. In contrast, in the transverse direction we consistently observe a single period (half-wave of the electric field) across the width of the mesa at all currents. This transverse variation which has been expected on the basis of observed emission characteristics and theoretical models has nevertheless eluded thus far a direct detection. Thus, the LTSLM patterns shown in Figure 2 on first sight indicate modes of the (n, 1, m_y)-type. The observed patterns are characterized by extrema along the center line and low amplitude around the perimeter. This is confirmed by Figure 3, which shows sections of the LTSLM image at 75 K, 15.25 mA, for which the amplitude of the oscillations decreases with increasing distance away from the long axis of the mesa.

These observed patterns do not, however, agree with expectations. It is possible to theoretically predict the LTSLM voltage response from a local temperature perturbation, for a THz device oscillating in steady state with a single cavity mode being excited. In the Appendix, we consider in detail the expected LTSLM patterns for perturbations to different parameters of the material. One can distinguish two basic types of patterns. The first type is related to the perturbation of the *c*-axis parameters, namely the Josephson current density, j_J, and *c*-axis quasiparticle conductivity, σ_c. In this case, the response follows the spatial distribution of the oscillating z component of the electric field. For example, for the cavity mode with wavevectors $k_i = \pi m_i / L_i$ ($i = x, y$), the voltage response to a local perturbation at point (x_0, y_0) should follow $\cos^2(k_x x_0)\cos^2(k_y y_0)$ for perturbation of σ_c, and $|\cos(k_x x_0)||\cos(k_y y_0)|$ for perturbation of j_J. The second type of the response pattern is related to the perturbation of the in-plane parameters, namely the London penetration depth λ_{ab}, and the *ab*-plane quasiparticle conductivity, σ_{ab}. In this case the response follows the

spatial distribution of the oscillating in-plane magnetic field and is proportional to $k_x^2 \sin^2(k_x x_0)\cos^2(k_y y_0) + k_y^2 \cos^2(k_x x_0)\sin^2(k_y y_0)$. However, *we cannot assign any of these basic patterns to the experimentally observed ones*. Since we observe oscillations in both directions, the only feasible candidate single mode is of type (n, 1, m_y). However, neither *c*-axis nor in-plane responses of this mode describe the experimental patterns. Indeed, patterns due to perturbations of out-of-plane material parameters have maxima of $|E_z|$, which occur around the perimeter of the cavity. Patterns due to perturbations of in-plane parameters reflect the distribution of $B_x^2 + B_y^2$, which has exactly the same oscillation amplitude at the center and along the edges (see Figure 1). By contrast, the patterns shown in Figure 2(c) consistently have very strong oscillations along the centerline of the mesa and weakest oscillations along the perimeter. We observed the same mode structure as shown in Fig. 2 on a second mesa patterned onto the same base crystal, see Fig. A2 in the Appendix. This second mesa has dimensions of 360 × 50 × 0.79 μm^3. We therefore conclude that the observed behavior is intrinsic to well heat-sunk BSCCO resonators and is robust to variations in device dimensions of up to 20%. Mode patterns displaying the expected geometry with extrema at the edges have previously been observed in single Nb junctions [28, 29].

A possible interpretation of the observed patterns is based on the assumption that *two* cavity modes are being excited simultaneously, forming a composite mode. Figure 5 compares the experimental LTSLM pattern seen at 15.25 mA with the function $\sin^2(\pi x)\cos^2(\pi y) + \cos^2(\pi x)\sin^2(\pi y) - 1.2\sin^2(\pi y)$ which describes the combination of the two theoretical in-plane response patterns corresponding to the cavity modes of (n, 0, m_y) and (n, 1, m_y) structure. Our addition of the squares of the mode amplitudes reflects a π/2 phase shift between their oscillations. Both modes combine into a single composite mode as evidenced by a single overall emission frequency of ~396 GHz at 15.00 mA (see Figure 6) even though

the two modes would have different center frequencies when excited independently of each other (see below). This interpretation is consistent with results recently obtained by Elarabi *et al.* [15,16] in which circularly polarized THz radiation was generated from a square mesa which had two corners truncated or from a circular mesa with notches, respectively, in diagonally opposite locations. This introduced a frequency difference of approximately 5% between the (1, 1) and (1, -1) mode resonances, which could then be excited simultaneously and a constant $\pi/2$ phase shift between them, resulting in circular polarization of the emitted radiation. (The signs of the indices associated with each mode component become important when the mesa lacks reflection symmetry about its centerlines, as is the case in reference [15].) These modes were phase-locked via mutual electromagnetic coupling to the cavity THz resonance associated with the shape of the mesa, as was theoretically predicted in [30].

A quantitative analysis of our results according to Equations 2 and 3 requires the specification of the boundary conditions and of the indices n, m_x and m_y, and is hampered by the complicated structure of our sample (see Fig. 1). The nature of the *c*-axis modes near the top of the mesa depends on the properties of the metal contact. Thick, high-conductivity metal contacts on the mesa induce an anti-node in the oscillating *c*-axis electric field, while thin contacts, such as used in this study, have typically low conductivity [31] likely resulting in a node at the top of the mesa. Due to losses in a thick base-crystal, the bottom of the *c*-axis electric-field mode profile is well approximated by a node [32]. However, since the base crystal in our case is only 100 nm thick we approximate the boundary condition at the bottom of the mesa with the behavior at the bottom of the sample, i.e., an anti-node. Thus, allowed values of n in the section under the thin Au-contact are 1, 3, … while under the thick contact we have 0, 2, … as depicted in Fig. 1. We note though that this classification in terms of the limiting cases, i.e., node or anti-node, is approximate, whereas the true behavior likely falls in

between with the thin contact being closer to a node while the thick contact is closer to an anti-node. Considering the CuO_2-planes as equipotentials across the entire mesa implies that the oscillation frequency is the same in both sections. A noticeable difference in the mode velocities in the two parts of the mesa perturbs the longitudinal mode structure. In addition, as can be seen in Fig. 5, at the left-hand end of the mesa there is neither a node nor an antinode. Thus, as mentioned above, the index m_y in Eq. (3) should be understood in our case as the non-integer ratio $2l/\Lambda_y$, where Λ_y is the longitudinal wavelength imaged in Fig. 2.

Anukool *et al*. [33] have measured $\lambda_{ab} = 0.47\,\mu m$ for optimally-doped Bi-2212 at 75 K. From the pattern periods, we evaluate $\Lambda_y/2 \approx 68$ μm ($m_y \approx 5.3$) and 61 μm ($m_y \approx 5.9$) for bias currents of 15 mA and 15.75 mA, respectively. Then, using $t = 0.992$ μm, $\varepsilon_c = 16$ [34], w = 60 μm and n = 1, 3 in Eqs. (2) and (3), we estimate the expected relevant cavity-mode frequencies for the imaged section at 75 K and summarize them in Table 1. As shown in Fig. 6, we observe a single instrument-resolution limited emission line at 396 GHz at a bias current of 15 mA, and at 440 GHz at 15.75 mA, which is broadly consistent with the excitation of a composite mode combining the (1, 0, m_y) and (3, 1, m_y) modes, respectively, with a π/2 phase shift. As the quality factor of the cavity resonances is relatively low, modes with rather large frequency differential can be simultaneously excited; however, further work is required to explore the mechanisms underlying the locking of the two modes and the selection of a π/2-phase shift.

We note that the total angle-integrated THz power emitted from the mesa studied here is comparatively weak at approximately 1.4 μW. (For details of our THz power calibration methodology, see Ref. [9]). This may be expected since the excitation of multiple modes, both of which contain multiple periods along the length of the mesa, would result in a THz-frequency electric field largely cancelling itself out in the far-field limit. By contrast, we find

that other optimally-doped mesas with similar width and height – but with a thicker 100 nm Au top electrode – can be driven to emit far more strongly at THz frequencies [35] under the same experimental conditions. As mentioned above, the properties of the top contact have a strong influence on losses and the *c*-axis mode structure. In addition, the contact arrangement consisting of thin and thick sections breaks the symmetry of the mesa. A systematic study as to whether these issues affect the formation of composite modes and the polarization state is underway.

The unexpected standing-wave structure observed here is unambiguously due to cavity resonance effects, for two reasons. Firstly, the strong pattern observed in the LTSLM images is not associated with a non-uniform temperature of the mesa. Figure 2(d) shows thermal maps of the mesa taken under the same conditions as the LTSLM images, using a thermoluminescent technique which measures the sample surface temperature directly. (For more details of this technique, see Refs. [25], [35], [36]). No oscillations are visible above the level of the noise in the thermoluminescent image (± 50 to 100 mK) meaning that the spatial oscillations in the LTSLM signal *cannot* be due to a spatial oscillation in the mesa surface temperature. Secondly, at certain bias currents and certain (*x*, *y*) coordinates, the LTSLM signal becomes *positive*. (See Fig. 4.) This can only be explained in terms of a cavity resonance pattern rather than periodic hot spots, since in a Bi-2212 mesa with $\partial\sigma_c/\partial T > 0$ whose electrical resistance is dominated by its *c*-axis current transport, local self-heating by the laser beam can only cause a *negative* perturbation of the device resistance. Interestingly, this result also suggests that a local rise in temperature in some places can enhance the cavity mode. Such a phenomenon in turn implies that thermal non-uniformity may serve as a potential means of enhancing the efficiency of IJJ synchronization in these stacks, which is consistent with previous theoretical [37] and experimental [38, 39] studies. No oscillatory

features are seen in the scanning laser images for $T_{bath} < 65$ K, at which temperatures no THz emission is detected from this mesa either.

Conclusions

Using low-temperature scanning laser microscopy and thermoluminescent imaging, we have studied the behavior of cavity resonance modes at around 0.4 THz of a stack of 640 Bi-2212 intrinsic Josephson junctions. We find that standing wave-like patterns are observed in the scanning laser images when – and only when – THz emission is detected from the mesa. While these patterns display varying behavior along the long axis of the mesa depending on the bias voltage, they consistently show a single half-period across the short axis of the mesa. This variation along the short axis which is assumed in most theoretical descriptions has not been clearly observed before. Comparison with thermoluminescent images of the device temperature under the same bias conditions also confirms that the LTSLM images reveal the nodes and antinodes of the mesa's electromagnetic cavity resonance modes, and not an inhomogeneous device temperature.

In conjunction with a detailed theoretical analysis of the contrast formation in LTSLM, our results also suggest that a composite mode consisting of two locked cavity modes with a $\pi/2$ phase shift is being excited. This mode generates a single sharp emission line at 396 GHz. The LTSLM patterns which we observe cannot be reconciled with excitation of a single cavity mode. Recent observations on asymmetric mesas [15,16] have indicated the formation of locked modes, however, the mechanisms underlying this unexpected behavior await further clarification. We note though, that the additional losses caused by the thin Au top electrode required for LTSLM and the broken symmetry may strongly affect the mode structure. Our work highlights aspects such as the properties of current contacts and the

selection of the mode structure that are important for optimizing the THz emission power from future IJJ-based devices.

Acknowledgements

Work at Argonne National Laboratory was funded by the US Department of Energy, Office of Science, Basic Energy Sciences, which also funds Argonne's Center for Nanoscale Materials (CNM) where the patterning of the BSCCO mesa was performed. We thank R. Divan for her help with sample fabrication. We would also like to acknowledge funding from the Deutsche Forschungsgemeinschaft (Project KL 930/13-1), and from the Japanese Society for the Promotion of Science.

References

[1] U. Welp, K. Kadowaki and R. Kleiner, Superconducting emitters of THz radiation, Nature Photonics **7**, 702 (2013); I. Kakeya, H. B. Wang, Terahertz-wave emission from Bi2212 intrinsic Josephson junctions: a review on recent progress, Supercond. Sci. Technol. **29**, 073001 (2016); T. Kashiwagi, H. Kubo, K. Sakamoto et al., The present status of high-T_c superconducting terahertz emitters, Supercond. Sci. Technol. **30**, 074008 (2017).

[2] Special issue "T-ray imaging, sensing, & detection" Proceedings of the IEEE **95**, nr. 8 (2007); M. Tonouchi, Nature Photonics **1**, 97 (2007); A. Redo-Sanchez and X.-C. Zhang, IEEE J. Sel. Top. Quantum Electron. **14**, 260 (2008).

[3] S. S. Dhillon, M. S. Vitiello, E. H. Linfield, *et al*., The 2017 THz science and technology road map, J. Phys. D: Appl. Phys. **50**, 043001 (2017).

[4] H. Sun, Z. Yang, N. V. Kinev et al., Terahertz Spectroscopy of Dilute Gases Using $Bi_2Sr_2CaCu_2O_{8+\delta}$ Intrinsic Josephson-Junction Stacks, Phys. Rev. Applied **8**, 054005 (2017).

[5] R. Kleiner, F. Steinmeyer, G. Kunkel and P. Müller, Intrinsic Josephson Effects in $Bi_2Sr_2CaCu_2O_8$ Single Crystals, Phys. Rev. Lett. **68**, 2394 (1992).

[6] A. E. Koshelev and L. N. Bulaevskii, Resonant electromagnetic emission from intrinsic Josephson-junction stacks with laterally modulated Josephson critical current, Phys. Rev. B **77**, 014530 (2008).

[7] L. Ozyuzer, A. E. Koshelev, C. Kurter et al., Emission of coherent THz radiation from superconductors, Science **318**, 1291 (2007).

[8] L. N. Bulaevskii, D. Dominguez, M. P. Maley and A. R. Bishop, Collective mode and the c-axis critical current of a Josephson-coupled superconductor at high parallel magnetic fields, Phys. Rev. B **53**, 14601 (1996).

[9] T. M. Benseman, K. E. Gray, A. E. Koshelev, W.-K. Kwok, U. Welp, H. Minami, K. Kadowaki and T. Yamamoto, Powerful terahertz emission from $Bi_2Sr_2CaCu_2O_{8+\delta}$ mesa arrays, Appl. Phys. Lett. **103**, 022602 (2013).

[10] T. Kashiwagi, T. Yamamoto, T. Kitamura et al., Generation of electromagnetic waves from 0.3 to 1.6 terahertz with a high-T_c superconducting $Bi_2Sr_2CaCu_2O_{8+\delta}$ intrinsic Josephson junction emitter, Appl. Phys. Lett. **106**, 092601 (2015).

[11] T. Kashiwagi, K. Sakamoto, H. Kubo et al., A high-T_c intrinsic Josephson junction emitter tunable from 0.5 to 2.4 terahertz, Appl. Phys. Lett. **107**, 082601 (2015).

[12] T. Kashiwagi, M. Tsujimoto, T. Yamamoto et al., High Temperature Superconductor Terahertz Emitters: Fundamental Physics and Its Applications, Japanese Journal of Applied Physics **51**, 010113 (2012).

[13] M. Tsujimoto, K. Yamaki, K. Deguchi, T. Yamamoto, T. Kashiwagi, H. Minami, M. Tachiki, K. Kadowaki and R. A. Klemm, Geometrical Resonance Conditions for THz Radiation from the Intrinsic Josephson Junctionsin $Bi_2Sr_2CaCu_2O_{8-d}$, Phys. Rev. Letters **105**, 037005 (2010).

[14] K. Delfanazari, H. Asai, M. Tsujimoto, T. Kashiwagi, T. Kitamura, T. Yamamoto, W. Wilson, R. A. Klemm, T. Hattori and K. Kadowaki, Effect of Bias Electrode Position on Terahertz Radiation From Pentagonal Mesas of Superconducting $Bi_2Sr_2CaCu_2O_{8+\delta}$, IEEE Transactions on Terahertz Science and Technology **5**, 505 (2015).

[15] A. Elarabi, Y. Yoshioka, M. Tsujimoto, I. Kakeya, Monolithic Superconducting Emitter of Tunable Circularly Polarized Terahertz Radiation, Phys. Rev. Applied **8**, 064034 (2017).

[16] A. Elarabi, Y. Yoshioka, M. Tsujimoto and I. Kakeya, Circularly polarized terahertz radiation monolithically generated by cylindrical mesas of intrinsic Josephson junctions, Appl. Phys. Lett. **113**, 052601 (2018).

[17] E. A. Borodianskyi and V. M. Krasnov, Josephson emission with frequency span 1–11 THz from small $Bi_2Sr_2CaCu_2O_{8+\delta}$ mesa structures, Nature Commun. **18**, 1742 (2017).

[18] R. Kleiner, Two-dimensional resonant modes in stacked Josephson junctions, Phys. Rev. B **50**, 6919 (1994); L. N. Bulaevskii, M. Zamora, D. Baeriswyl, H. Beck and J. R. Clem, Time-dependent equations for phase differences and a collective mode in Josephson-coupled layered superconductors, Phys. Rev. B **50**, 12831 (1994); S. Sakai, A. V. Ustinov, H. Kohlstedt, A. Petraglia and N. F. Pedersen, Theory and experiment on electromagnetic-wave-propagation velocities in stacked superconducting tunnel structures, Phys. Rev. B **50**, 12905 (1994); N. F. Pedersen and S. Sakai, Josephson plasma resonance in superconducting multilayers, Phys. Rev. B **58**, 2820 (1998).

[19] T. M. Benseman, A. E. Koshelev, K. E. Gray, W.-K. Kwok, U. Welp, K. Kadowaki, M. Tachiki and T. Yamamoto, Tunable terahertz emission from $Bi_2Sr_2CaCu_2O_{8+\delta}$ mesa devices, Phys. Rev. B **84**, 064523 (2011).

[20] T. Kashiwagi, T. Yuasa, Y. Tanabe et al., Improved excitation mode selectivity of high-temperature superconducting terahertz emitters, J. Appl. Phys. **124**, 033901 (2018).

[21] H. Minami, I. Kakeya, H. Yamaguchi, T. Yamamoto and K. Kadowaki, Characteristics of terahertz radiation emitted from the intrinsic Josephson junctions in high-T_c superconductor $Bi_2Sr_2CaCu_2O_{8+\delta}$, Appl. Phys. Lett. **95**, 232511 (2009).

[22] H. B. Wang, S. Guenon, J. Yuan, A. Iishi, S. Arisawa, T. Hatano, T. Yamashita, D. Koelle, and R. Kleiner, Hot Spots and Waves in $Bi_2Sr_2CaCu_2O_8$ Intrinsic Josephson Junction Stacks: A Study by Low Temperature Scanning Laser Microscopy, Phys. Rev. Lett. **102**, 017006 (2009).

[23] H. B. Wang, S. Guenon, B. Gross et al., Coherent Terahertz Emission of Intrinsic Josephson Junction Stacks in the Hot Spot Regime, Phys. Rev. Lett. **105**, 057002 (2010).

[24] S. Guénon, M. Grünzweig, B. Gross et al., Interaction of hot spots and terahertz waves in $Bi_2Sr_2CaCu_2O_8$ intrinsic Josephson junction stacks of various geometry, Phys. Rev. B **82**, 214506 (2010).

[25] B. Gross, S. Guénon, J. Yuan et al., Hot-spot formation in stacks of intrinsic Josephson junctions in $Bi_2Sr_2CaCu_2O_8$, Phys. Rev. B **86**, 094524 (2012).

[26] T. M. Benseman, A. E. Koshelev, V. Vlasko-Vlasov et al., Current Filamentation in Large $Bi_2Sr_2CaCu_2O_{8+\delta}$ Mesa Devices Observed via Luminescent and Scanning Laser Thermal Microscopy, Phys. Rev. Applied **3**, 044017 (2015).

[27] S. Guénon, M. Grünzweig, B. Gross et al., Interaction of hot spots and terahertz waves in $Bi_2Sr_2CaCu_2O_8$ intrinsic Josephson junction stacks of various geometry, Phys. Rev. B **82**, 212506 (2010).

[28] B. Mayer, T. Doderer, R. P. Huebener, A. V. Ustinov, Phys. Rev. B **44**, 12463 (1991).

[29] S. G. Lachenmann, T. Doderer, R. P. Huebener, D. Quenter, J. Niemeyer and R. Pöpel, Phys. Rev. B **48**, 3295 (1993).

[30] H. Asai and S. Kawabata, Emission of Circularly Polarized Terahertz Wave from Inhomogeneous Intrinsic Josephson Junctions, IEEE Trans. Applied Superconductivity **26**, 1800804 (2016).

[31] J. W. C. de Vries, Resistivity of thin Au-films as a function of grain diameter and temperature, J. Phys. F: Met. Phys. **17**, 1945 (1987); J. W. C. de Vries, Temperature and thickness dependence of the resistivity of thin polycrystalline Aluminium, Cobalt, Nickel, Palladium and Gold Films, Thin Solid Films **167**, 25 (1988); T. H. Gilani, D. Rabchuk, Electrical resistivity of gold thin film as a function of film thickness, Can. J. Phys. **96**, 272 (2018).

[32] A. E. Koshelev and L. N. Bulaevskii, Resonant Terahertz Radiation from Layered Superconductors: Mechanisms of Damping and Structure of Dynamic States, Journal of Physics: Conference Series **150**, 052124 (2009).

[33] W. Anukool, S. Barakat, C. Panagopoulos and J. R. Cooper, Effect of hole doping on the London penetration depth in $Bi_{2.15}Sr_{1.85}CaCu_2O_{8+\delta}$ and $Bi_{2.1}Sr_{1.9}Ca_{0.85}Y_{0.15}Cu_2O_{8+\delta}$, Phys. Rev. B **80**, 024516 (2009).

[34] K. Delfanazari, H. Asai, M. Tsujimoto et al., Tunable terahertz emission from the intrinsic Josephson junctions in acute isosceles triangular $Bi_2Sr_2CaCu_2O_{8+\delta}$ mesas, Optics Express **21**, 2171 (2013).

[35] T. M. Benseman, A. E. Koshelev, W.-K. Kwok, U. Welp, V. K. Vlasko-Vlasov, K. Kadowaki, H. Minami and C. Watanabe, Direct imaging of hot spots in $Bi_2Sr_2CaCu_2O_{8+\delta}$ mesa terahertz sources, J. Appl. Phys. **113**, 133902 (2013).

[36] P. Kolodner and J. A. Tyson, Microscopic fluorescent imaging of surface temperature profiles with 0.01 °C resolution, Appl. Phys. Lett. **40**, 782 (1982); P. Kolodner and J. A. Tyson, Remote thermal imaging with 0.7-μm spatial resolution using temperature-dependent fluorescent thin films, Appl. Phys. Lett. **42**, 117 (1983); G. Hampel, P. Kolodner, P. L. Gammel et al., High power failure of superconducting microwave filters: Investigation by means of thermal imaging, Appl. Phys. Lett. **69**, 571 (1996); O. Haugen, T. H. Johansen, H. Chen, V. Yurchenko, P. Vase, D. Winkler, B. A. Davidson, G. Testa, E. Sarnelli and E. Altshuler, High Resolution Thermal Imaging of Hotspots in Superconducting Films, IEEE Trans. Appl. Supercond. **17**, 3215 (2007); S. Niratisairak, O. Haugen, T. H. Johansen and T. Ishibashi, Observation of hotspot in BSCCO thin film structure by fluorescent thermal imaging, Physica C **468**, 442 (2008).

[37] A. Yurgens, Temperature distribution in a large $Bi_2Sr_2CaCu_2O_{8+\delta}$ mesa, Phys. Rev. B **83**, 184501 (2011).

[38] C. Watanabe, H. Minami, T. Yamamoto, T. Kashiwagi, R. A. Klemm and K. Kadowaki, Spectral investigation of hot spot and cavity resonance effects on the terahertz radiation from high-T_c superconducting $Bi_2Sr_2CaCu_2O_{8+\delta}$ mesas, J. Phys.: Condens. Matter **26**, 172201 (2014).

[39] M. Tsujimoto, H. Kambara, Y. Maeda, Y. Yoshioka, Y. Nakagawa and I. Kakeya, Dynamic Control of Temperature Distributions in Stacks of Intrinsic Josephson Junctions in $Bi_2Sr_2CaCu_2O_{8+\delta}$ for Intense Terahertz Radiation, Phys. Rev. Applied **2**, 044016 (2014).

[40] A. E. Koshelev, Alternating dynamic state self-generated by internal resonance in stacks of intrinsic Josephson junctions, Phys. Rev. B **78**, 174509 (2008).

[41] S. Z. Lin and X. Hu, Possible Dynamic States in Inductively Coupled Intrinsic Josephson Junctions of Layered High-T_c Superconductors, Phys. Rev. Lett. **100**, 247006 (2008).

Table 1

$\Lambda_y/2$ [μm]	m_y	(1, 0, m_y)	(3, 0, m_y)	(1, 1, m_y)	(3, 1, m_y)
68	5.3	456.5 GHz	243.7 GHz	690 GHz	368.3 GHz
61	5.9	508.9 GHz	271.7 GHz	725.8 GHz	387.4 GHz

Estimated cavity-mode frequencies, Eq. (3), for a mesa of size $60 \times 360 \times 0.992$ μm^3, $\varepsilon_c = 16$, $\lambda_{ab} = 0.47$ μm, and two measured LTSLM periods, $\Lambda_y/2$, with $m_y = 2l/\Lambda_y$.

Figure captions

Figure 1 (Color online only)

Schematic of the BSCCO mesa imaged here and of possible *c*-axis mode profiles.

Figure 2 (Two-column figure, Color online only)

(a) (Main) Resistance versus temperature plotted for the mesa studied in this experiment. Red curve was measured directly with 10 μA bias current, while blue squares for data points below T_c were obtained from the tangent to downward-sweep *I-V* curves (black line in inset) as described in [26]. (Inset) *I-V* characteristic for mesa at 75 K showing hysteretic switching of IJJs. THz emission occurs on downward sweep.

(b) Enlargement of region enclosed in dotted red box in (a). Vertical axis shows mesa bias current, while voltage and total radiated THz power are plotted on horizontal axes.

(c) Maps of position-dependent scanning laser signal, showing signed RMS perturbation to mesa voltages at a range of bias currents, and a bath temperature of 75 K. Red dashed lines show cross-sections plotted in Figures 3 and 4.

(d) Conventional optical image of mesa at top (with 500 nm Au current electrode on right) and direct thermoluminescent images of mesa under same conditions as measured in (c).

Figure 3 (Color online only)

(a) Longitudinal cross-sections of scanning laser signal data plotted in Fig. 2c along centerline of mesa (red dashed line in Fig. 2c) showing strong positive and negative oscillations at bias currents for which the mesa's cavity resonance is excited, and T_{bath} = 75 K.

(b) Equivalent cross-sections for thermoluminescent data, indicating absence of corresponding oscillations in the mesa temperature itself. Vertical dashed lines show locations of thermal imaging artifacts due to reflection of light from the sidewalls of the mesa and its 500 nm-thick Au current electrode. Note that the temperature rise observed here is not very large compared with the noise floor of this technique. The steep rise in the temperature profiles starting near 450 μm is caused by Joule heating in the contact. At this point the gold film transitions onto an epoxy ramp leading to contact pads further out. Due to the reduced thermal conductivity of the epoxy the temperature rises rapidly.

Figure 4 (Color online only)

(a) Longitudinal cross-sections of scanning laser image for T_{bath} = 75 K, I = 15.25 mA, taken at increasing distance from the centerline of the mesa. The amplitude of the oscillations strongly decreases as the edge of the mesa is approached, indicating that the cavity mode being excited has a significant transversal component.

(b) Transverse cross-sections of the LTSLM image for T_{bath} = 75 K taken at increasing bias current. These cross-sections were taken through the minimum of the LTSLM pattern which occurs at x = 130 μm, indicated by the arrow in Figure 4(a).

Figure 5 (Color online only)

(Top) Section of the experimental LTSLM pattern seen at T_{bath} = 75 K, I = 15.25 mA, as compared with the function $\sin^2(\pi x)\cos^2(\pi y) + \cos^2(\pi x)\sin^2(\pi y) - 1.2\sin^2(\pi y)$ (Bottom). This function approximates the sum of the two theoretical in-plane response patterns for perturbations of the *in*-plane parameters, corresponding to the cavity modes (0, m) and (1, m).

Figure 6 (Color online only)

FTIR spectra emitted by the mesa at its highest achievable THz power output, which occurred at T_{bath} = 75 K, I = 15.00 mA, and also at the closest local maximum of emitted power with respect to bias current, which occurred at 15.75 mA. The total emitted power (radiated over all angles) at 15.00 mA is approximately 1.4 μW, while the center frequency is 396 GHz. The observed linewidth at 15.00 mA is limited by the spectrometer resolution at 0.75 cm^{-1}, or 2.25 GHz. At 15.75 mA, the emission linewidth becomes broader, and possibly multi-peaked. The satellite peaks, however, are difficult to definitively distinguish from background noise. (Two spectra taken at 15.75 mA are plotted as an indication of the level of reproducibility of these spectra.)

Figure A1 (Color online only)

Typical spatial patterns corresponding to the c-axis (σ_c and j_J) and in-plane response channels for three different modes. We note that all of these patterns have maxima / minima at the edges of the sample, in contrast with what we observe experimentally.

Figure A2 (Two-column figure, Color online only)

(a) *I-V* characteristic for a second mesa patterned on the same chip as the mesa presented in the main text, at 75 K showing hysteretic switching of IJJs. THz emission occurs on downward sweep.

(b) Enlargement of region enclosed in dotted red box in (a). Vertical axis shows mesa bias current, while voltage and total radiated THz power are plotted on horizontal axes.

(c) Maps of position-dependent scanning laser signal, showing signed RMS perturbation to mesa voltages at a range of bias currents, and a bath temperature of 75 K. The signal magnitude is slightly larger than it is for the data in Figure 2(c), due to the higher ratio of laser-heated spot volume to mesa volume for this mesa. The top panel shows an optical image of the mesa (with 500 nm Au current electrode on right).

Figure A3 (Two-column figure, Color online only)

(a) Current-Voltage characteristic and THz emission data at T_{bath} = 65 K, for the same mesa as shown in Figure 2 in the main text. Vertical axis shows mesa bias current, while voltage and total radiated THz power are plotted on horizontal axes.

(b) Maps of position-dependent scanning laser signal, showing signed RMS perturbation to mesa voltages at a range of bias currents, and a bath temperature of 65 K.

(c) Conventional optical image of mesa at top (with 500 nm Au current electrode on right) and direct thermoluminescent images of mesa under same conditions as measured in (b).

Figure A4 (Color online only)

Detail of downward-sweep current-voltage characteristics in the regions at which THz emission occurred at T_{bath} = 75 K. Current-voltage characteristics show good agreement between the three cryostat systems in which the devices were measured, with only minor shifts due to small variations in thermometer calibration. Curves measured in the scanning laser imaging system (purple solid lines) are plotted for the time-averaged DC voltage while the sample is illuminated by the laser beam. Note that these curves show a slightly higher retrapping current as compared to the other systems, due to laser-spot induced heating causing an increased probability of Josephson retrapping.

Appendix

Response to local perturbation for cavity modes in Josephson-junction stacks

In this section we give a detailed analysis of the effect of perturbations of the temperature distribution on the Josephson dynamics. Several mechanisms can give rise to changes in the temperature distribution.

Self-heating arises due to Joule heating throughout the volume of the sample which is largely controlled by the efficiency of heat removal. In our case, heat removal is very effective, and self-heating is comparatively weak. Self-heating is essentially uniform across the sample as directly measured in the thermal images. Under biasing conditions for which THz emission was seen, self-heating of the device was 0.6 Kelvin or less. However, under certain conditions of Joule heating, heat removal, temperature dependence of the conductivity, etc., the uniformly heated state becomes unstable and hot spots form [23-27]. Hot spot states do not arise in the devices studied in this manuscript, since the mesas were purposely designed to avoid such phenomena co-existing with THz emission modes.

In contrast, in LTLSM local heating is imparted by the focused laser spot. The resulting local temperature rise will be reduced by effective heat removal. However, since the laser spot power density per unit area is about 100 times greater than the overall DC power density in the mesa, even in well heat-sunk samples a time-modulated signal arises which is easily measurable via AC detection techniques. We estimate for the current operating conditions a local temperature rise of about 2 K.

In the following theoretical analysis assume that a laser spot heats up a mesa in the vicinity of coordinate $\mathbf{r}_0$ leading to local variations of the materials parameters: the components of the quasiparticle conductivity, σ_{ab} and σ_c, the in-plane London penetration depth, λ, and the Josephson current density, j_J. In the simplest picture, such parameter variation can be

evaluated as $\tilde{a}(\mathbf{r}) = \tilde{a}_0\, f_T(\mathbf{r}-\mathbf{r}_0)$, where $\tilde{a}_0 = \frac{da}{dT}\Delta\mathrm{T}$ for $a = \sigma_{ab}, \sigma_c, \lambda^{-2}, j_J$, ΔT is the temperature increase in the spot center, and the dimensionless function $f_T(\mathbf{r})$ describes the temperature-enhancement decay away from the spot, $f_T(0) = 1$. The variations of the local parameters lead to a change in the DC bias voltage, which we can represent as

$$\Delta V(\mathbf{r}_0) = \sum_a \mathcal{R}_{V,a}(\mathbf{r}_0)\frac{\tilde{a}_0}{a},$$

where the sum is over all of the above parameters. The goal of this appendix is to evaluate the response functions $\mathcal{R}_{V,a}(\mathbf{r}_0)$ for a simple situation when only one cavity mode is excited inside the mesa. Theoretically, it is more convenient to evaluate the current responses at fixed voltage, $\mathcal{R}_{j,a}(\mathbf{r}_0)$. The two response functions are connected by the simple relation, $\mathcal{R}_{V,a}(\mathbf{r}_0) = \frac{dV}{dj}\mathcal{R}_{j,a}(\mathbf{r}_0)$.

1. Phase dynamics and I-V dependence for cavity modes

We consider a finite-size stack (mesa) containing N junctions with lateral sizes L_x and L_y. The dynamic behavior of the intrinsic Josephson-junction stacks can be described by the coupled equations for the c-axis electric field E_n, phase θ_n, in-plane magnetic field $\mathbf{H}_n = (H_{x,n}, H_{y,n})$ in the junction with index n, and the in-plane superconducting momentum $\mathbf{p}_n = (p_{x,n}, p_{y,n})$ in the n^{th} layer, see e.g. Refs. [39] and [40]

$$\frac{\varepsilon_c}{c}\frac{\partial E_n}{\partial t} + \frac{4\pi}{c}\left(\sigma_c E_n + j_J \sin\theta_n\right) = \frac{\partial H_{y,n}}{\partial x} - \frac{\partial H_{x,n}}{\partial y} \quad (1)$$

$$\frac{\partial \theta_n}{\partial t} = \frac{2\pi c s E_n}{\Phi_0} \quad (2)$$

$$\frac{4\pi}{c}\left(\sigma_{ab}\frac{\Phi_0}{2\pi c}\frac{\partial p_{i,n}}{\partial t} + \frac{c\Phi_0}{8\pi^2\lambda^2}p_{i,n}\right) = -e_{ijz}\frac{H_{j,n}-H_{j,n-1}}{s} \quad (3)$$

$$\frac{2\pi s}{\Phi_0}H_{j,n} = e_{ijz}\left(\frac{\partial\theta_n}{\partial r_i} - p_{i,n+1} + p_{i,n}\right) \quad (4)$$

with the in-plane coordinate $\mathbf{r} = (r_1, r_2) = (x, y)$, $0 < r_i < L_i$ and the Levi-Civita symbol e_{ijk} ($e_{xyz} = -e_{yxz} = 1$). For completeness, we consider first the well-known unperturbed solution in the resonance steady state when the dynamic kink state is formed [40, 41] leading to excitation of a single cavity mode. We will look for a solution for the phase in the form

$$\theta_n(\mathbf{r}, t) = \omega t + \theta_{k,n}(\mathbf{r}) + \phi_n(\mathbf{r}, t),$$

where $\omega = \frac{2\pi c}{\Phi_0}V$ is the Josephson frequency set by the DC voltage drop per junction V, $\theta_{k,n}(\mathbf{r}) = \theta_k(\mathbf{r}) + \beta_n$, $\theta_k(\mathbf{r})$ is the kink's phase, and β_n is the additional phase shifts that are required to maintain the current conservation between the junctions. The kinks provide the π phase shifts at the nodal lines of the oscillating electric fields, i. e., $\exp[i\theta_k(\mathbf{r})] \approx \mathrm{sgn}[\cos(k_x x)\cos(k_y y)]$ with $k_i = \pi m_i/L_i$. We will assume that the dynamic phases $\phi_n(\mathbf{r}, t)$ are small allowing us to use the expansion with respect to the Josephson current.

Using the complex presentation $A(t) = \mathrm{Re}[A\exp(i\omega t)]$ for the oscillating quantities, we obtain the following equations for these quantities

$$\frac{i\varepsilon_c\omega+4\pi\sigma_c}{c}E_n - \frac{\partial H_{yn}}{\partial x} + \frac{\partial H_{xn}}{\partial y} = \frac{4\pi}{c}j_J i\exp\left[i\theta_{k,n}(\mathbf{r})\right], \quad (5)$$

$$i\omega\phi_n = \frac{2\pi csE_n}{\Phi_0}, \quad (6)$$

$$\frac{4\pi}{c}\left(\sigma_{ab}\frac{\Phi_0}{2\pi c}i\omega + \frac{c\Phi_0}{8\pi^2\lambda^2}\right)p_{i,n} = -e_{ijz}\frac{H_{j,n}-H_{j,n-1}}{s}, \quad (7)$$

$$\frac{2\pi s}{\Phi_0}H_{j,n} = e_{ijz}\left(\frac{\partial\phi_n}{\partial r_i} - p_{i,n+1} + p_{i,n}\right), \quad (8)$$

where we used $-\sin\left(\omega t + \theta_{k,n}(\mathbf{r})\right) = \mathrm{Re}\left\{i\exp\left[i\left(\omega t + \theta_{k,n}(\mathbf{r})\right)\right]\right\}$ for the oscillating Josephson current. Eliminating the phase and in-plane momentum, we obtain equations containing only oscillating fields,

$$(i\varepsilon_c\omega + 4\pi\sigma_c)E_n - e_{ijz}c\frac{\partial H_{j,n}}{\partial r_i} = 4\pi j_J i\exp\left[i\theta_{k,n}(\mathbf{r})\right], \quad (9)$$

$$H_{j,n} - \frac{H_{j,n+1}+H_{j,n-1}-2H_{j,n}}{s^2 n_\lambda} = e_{ijz}\frac{c}{i\omega}\frac{\partial E_n}{\partial r_i}, \quad (10)$$

where we introduced the notation $n_\lambda \equiv \lambda^{-2} + \frac{4\pi i\omega\sigma_{ab}}{c^2}$. In the case when the Josephson frequency ω is close to the cavity-resonance frequency $[1+\lambda^2 k_z^2]^{-1/2}\frac{ck}{\sqrt{\varepsilon_c}}$ with $k_z^2 \equiv 2(1-\cos q)/s^2$ and $k = \sqrt{(m_x/L_x)^2 + (m_y/L_y)^2}$, the (m_x, m_y) mode corresponding to this resonance is mostly excited. Due to the large impedance mismatch between $Bi_2Sr_2CaCu_2O_8$ and free space, the in-plane gradients of the oscillating electric field almost vanish at the mesa's edges. Therefore, the coordinate dependences of the mode's oscillating fields can be approximated as

$$E_n(\mathbf{r}) \approx E_{\mathbf{k},q}\cos(k_x x)\cos\left(k_y y\right)\cos(qn+\alpha), \quad (11)$$

$$H_{y,n}(\mathbf{r}) \approx H_{y,\mathbf{k},q}\sin(k_x x)\cos\left(k_y y\right)\cos(qn+\alpha), \quad (12)$$

$$H_{x,n}(\mathbf{r}) \approx H_{x,\mathbf{k},q}\cos(k_x x)\sin\left(k_y y\right)\cos(qn+\alpha), \quad (13)$$

where the *c*-axis wave vector q and the phase factor α depend on the boundary conditions on the top and bottom of the mesa. The amplitudes can be evaluated by performing projection of Eqs. (9) and (10) to the mode shape. In particular, for the mode amplitude of the electric field we obtain

$$E_{\mathbf{k},q} \approx 4\pi j_J \omega g_{\mathbf{k},q} \left(\varepsilon_c \omega^2 - 4\pi i\omega\sigma_c - \frac{c^2k^2}{1+k_z^2/n_\lambda}\right)^{-1}, \quad (14)$$

where

$$g_{\mathbf{k},q} \approx \frac{4\eta_q}{L_x L_y N} \int_0^{L_x} |\cos(k_x x)|dx \int_0^{L_y} \left|\cos\left(k_y y\right)\right| dy \sum_{n=1}^{N} \cos(qn+\alpha)\exp(i\beta_n)$$

$$= \frac{16\eta_q}{\pi^2} \langle \cos(qn+\alpha)\exp(i\beta_n)\rangle_n \qquad (15)$$

is the mode's coupling constant and $\eta_q = \langle \cos^2(qn+\alpha)\rangle_n^{-1}$. The magnetic-field amplitudes are related to $E_{\mathbf{k},q}$ as

$$H_{j,\mathbf{k},q} = -e_{ijz}\left[1+\frac{k_z^2}{n_\lambda}\right]^{-1} \frac{ck_i}{i\omega} E_{\mathbf{k},q}. \qquad (16)$$

Note that the result in Eq. (14) assumes only the quasiparticle damping of the modes and neglects, for example, the damping due to leaking of the radiation into the base crystal.

The change of the current-voltage characteristic due to the excitation of the cavity mode is determined by the average Josephson current, which we can evaluate as

$$\overline{j_J} = j_J \left\langle \sin\left[\omega t + \theta_{k,n}(\mathbf{r}) + \phi_n(\mathbf{r},t)\right]\right\rangle_{\mathbf{r},t} \approx j_J \left\langle \cos\left[\omega t + \theta_{k,n}(\mathbf{r})\right] \mathrm{Re}[\phi_n(\mathbf{r})\exp(i\omega t)]\right\rangle_{\mathbf{r},t}$$

$$= \frac{j_J}{2} \mathrm{Re}\left\langle \exp\left[-i\theta_{k,n}(\mathbf{r})\right]\phi_n(\mathbf{r})\right\rangle_{\mathbf{r}} = \frac{2j_J}{\pi^2} \mathrm{Re}\left[\exp[-i\beta_n(\mathbf{r})]\cos(qn+\alpha)\phi_{\mathbf{k},q}\right], (17)$$

where we used $\left\langle \exp[-i\theta_k(\mathbf{r})]\cos(k_x x)\cos\left(k_y y\right)\right\rangle_{\mathbf{r}} \approx \left\langle |\cos(k_x x)|\left|\cos\left(k_y y\right)\right|\right\rangle_{\mathbf{r}} = 4/\pi^2$. The phase shifts β_n have to be selected to make this result independent of n. Averaging over n, we obtain

$$\overline{j_J} \approx \frac{j_J}{8\eta_q} \mathrm{Re}\left[\bar{g}_{\mathbf{k},q}\phi_{\mathbf{k},q}\right] \qquad (18)$$

As the oscillating phase is connected with the evaluated oscillating electric field in Eq. (14), $\phi_{\mathbf{k},q} = \frac{2\pi cs}{i\omega\Phi_0} E_{\mathbf{k},q}$, we immediately obtain the result for the average Josephson current [40, 41],

$$\overline{j_J} \approx \frac{\pi^2 cs}{\eta_q \Phi_0} \left|g_{\mathbf{k},q}\right|^2 j_J^2 \mathrm{Im}\left\{\varepsilon_c \omega^2 - 4\pi i\omega\sigma_c - \frac{c^2k^2}{1+k_z^2/n_\lambda}\right\}^{-1}, \tag{19}$$

which is resonantly enhanced when the cavity mode is excited. The full current-voltage relation is $j = \sigma_c E + \overline{j_J}$.

2. Response to small local perturbation

We can now proceed with the evaluation of the correction to the average Josephson current caused by perturbations induced by the laser spot near point $\mathbf{r}_0$, $\tilde{a}(\mathbf{r})$ with $a = \sigma_c$, σ_{ab}, j_J, λ^{-2}. Adding these perturbations to Eqs. (1), we obtain the following equations for the corrections:

$$\frac{i\omega\varepsilon_c + 4\pi\sigma_c}{c}\tilde{E}_n - \frac{\partial \tilde{H}_{yn}}{\partial x} + \frac{\partial \tilde{H}_{xn}}{\partial y} = -\frac{4\pi}{c}\left[\tilde{\sigma}_c E_n - \tilde{j}_J i\exp\left(i\theta_{k,n}\right)\right], \tag{20}$$

$$\tilde{\theta}_n = \frac{2\pi cs\tilde{E}_n}{i\omega\Phi_0}, \tag{21}$$

$$\frac{\Phi_0}{2\pi} n_\lambda \tilde{p}_{i,n} + e_{ijz}\frac{\tilde{H}_{j,n} - \tilde{H}_{j,n-1}}{s} = -\frac{\Phi_0}{2\pi}\tilde{n}_\lambda p_{i,n}, \tag{22}$$

$$\frac{2\pi s}{\Phi_0}\tilde{H}_{j,n} = e_{ijz}\left(\frac{\partial\tilde{\theta}_n}{\partial r_i} - \tilde{p}_{i,n+1} + \tilde{p}_{i,n}\right). \tag{23}$$

with $\tilde{n}_\lambda(\omega) \equiv \tilde{\lambda}^{-2} + \frac{4\pi i\omega}{c^2}\tilde{\sigma}_{ab}$. For brevity, we have omitted the coordinate dependences. Eliminating $\tilde{\theta}_n$ and $\tilde{p}_{i,n}$, we again obtain equations containing only the perturbations of the fields

$$\frac{i\omega\varepsilon_c + 4\pi\sigma_c}{c}\tilde{E}_n - \frac{\partial \tilde{H}_{yn}}{\partial x} + \frac{\partial \tilde{H}_{xn}}{\partial y} = -\frac{4\pi}{c}\left[\tilde{\sigma}_c E_n - \tilde{j}_J i\exp\left(i\theta_{k,n}\right)\right], \tag{24}$$

$$\tilde{H}_{j,n} - \frac{\tilde{H}_{j,n-1} + \tilde{H}_{j,n+1} - 2\tilde{H}_{j,n}}{n_\lambda s^2} - e_{ijz}\frac{c}{i\omega}\frac{\partial\tilde{E}_n}{\partial r_i} = e_{ijz}\frac{\tilde{n}_\lambda}{n_\lambda}\frac{\Phi_0}{2\pi s}\left(p_{i,n+1} - p_{i,n}\right). \tag{25}$$

The electric field E_n on the right-hand side of the first equation is given by Eqs. (11) and (14) and momenta differences are related to the oscillating magnetic fields

$$p_{i,n+1} - p_{i,n} = e_{imz}\frac{4\pi H_{m,n}(1-\cos q)}{s\Phi_0 n_\lambda}.$$

Even though the perturbations on the right-hand side of Eqs. (2) are localized near the laser spot point $\mathbf{r}_0$, due to proximity to the resonance, their dominating effect is the corrections of the cavity-mode amplitude. To evaluate these corrections, we again project Eqs. (2) to the cavity-mode shape. This leads to the following equations for the corrections to the mode amplitudes of the oscillating fields

$$\frac{i\omega\varepsilon_c+4\pi\sigma_c}{c}\tilde{E}_{\mathbf{k},q} - k_x\tilde{H}_{y,\mathbf{k},q} + k_y\tilde{H}_{x,\mathbf{k},q}$$

$$= -\frac{4\pi}{c}\frac{S_l}{L_xL_y}\left(\tilde{\sigma}_c E_{\mathbf{k},q}\cos^2(k_x x_0)\cos^2\left(k_y y_0\right) - i\tilde{j}_J r_q|\cos(k_x x_0)|\left|\cos\left(k_y y_0\right)\right|\right) \qquad (26)$$

$$\tilde{H}_{x,\mathbf{k},q}\left(1+\frac{k_z^2}{n_\lambda}\right) - \frac{ck_y}{i\omega}\tilde{E}_{\mathbf{k},q} = \frac{S_l}{L_xL_y}\frac{\tilde{n}_\lambda}{n_\lambda^2}H_{x,\mathbf{k},q}\cos^2(k_x x_0)\sin^2\left(k_y y_0\right)k_z^2 \qquad (27)$$

$$\tilde{H}_{y,\mathbf{k},q}\left(1+\frac{k_z^2}{n_\lambda}\right) + \frac{ck_x}{i\omega}\tilde{E}_{\mathbf{k},q} = \frac{S_l}{L_xL_y}\frac{\tilde{n}_\lambda}{n_\lambda^2}H_{y,\mathbf{k},q}\sin^2(k_x x_0)\cos^2\left(k_y y_0\right)k_z^2 \qquad (28)$$

where S_l is the area of the spot $\int d^2\mathbf{r}\tilde{a}(\mathbf{r}) = \tilde{a}S_l$ and $r_q = \eta_q\langle\exp(i\beta_n)\cos(qn+\alpha)\rangle_n$. From these equations we evaluate the correction to the mode's amplitude of the electric field

$$\tilde{E}_{\mathbf{k},q} = \frac{S_l}{L_xL_y}\left[\omega^2\varepsilon_c - 4\pi i\omega\sigma_c - \frac{c^2k^2}{1+\frac{k_z^2}{n_\lambda}}\right]^{-1}$$

$$\times\{4\pi i\omega\left(\tilde{\sigma}_c E_{\mathbf{k},q}\cos^2(k_x x_0)\cos^2\left(k_y y_0\right) - i\tilde{j}_J r_q|\cos(k_x x_0)|\left|\cos\left(k_y y_0\right)\right|\right)$$

$$+\frac{c^2\frac{k_z^2}{n_\lambda}}{\left(1+\frac{k_z^2}{n_\lambda}\right)^2}\frac{\tilde{n}_\lambda}{n_\lambda}\left[k_x^2\sin^2(k_x x_0)\cos^2\left(k_y y_0\right) + k_y^2\cos^2(k_x x_0)\sin^2\left(k_y y_0\right)\right]E_{\mathbf{k},q}\}, \qquad (29)$$

which immediately gives the perturbations of the oscillating-phase amplitude, $\tilde{\phi}_{\mathbf{k},q} = \frac{2\pi cs}{i\omega\Phi_0}\tilde{E}_{\mathbf{k},q}$ and the average Josephson current using Eq. (17),

$\overline{\delta j_J}(\mathbf{r}_0) \approx \frac{j_J}{8\eta_q}\mathrm{Re}\left[\bar{g}_{\mathbf{k},q}\tilde{\phi}_{\mathbf{k},q}\right]$. We can split the resulting change of the average Josephson current into the responses to relative perturbations of different parameters

$$\overline{\delta j_J}(\mathbf{r}_0) = \sum_a \mathcal{R}_{j,a}(\mathbf{r}_0)\frac{\tilde{a}}{a} \tag{30}$$

where

$$\mathcal{R}_{j,\sigma_c}(\mathbf{r}_0) = 4\pi\mathcal{A}_J\sigma_c\omega\left|g_{\mathbf{k},q}\right|^2\mathrm{Re}\left[\left(\omega^2\varepsilon_c - 4\pi i\omega\sigma_c - \frac{c^2k^2}{1+\frac{k_z^2}{n_\lambda}}\right)^{-2}\right]\cos^2(k_x x_0)\cos^2\left(k_y y_0\right), \tag{31}$$

$$\mathcal{R}_{j,j_J}(\mathbf{r}_0) = \mathcal{A}_J\mathrm{Im}\left[\frac{r_q\bar{g}_{\mathbf{k},q}}{\omega^2\varepsilon_c - 4\pi i\omega\sigma_c - \frac{c^2k^2}{1+\frac{k_z^2}{n_\lambda}}}\right]\left|\cos(k_x x_0)\right|\left|\cos\left(k_y y_0\right)\right|, \tag{32}$$

$$\mathcal{R}_{j,\lambda^{-2}}(\mathbf{r}_0) = \mathcal{A}_J c^2\left|g_{\mathbf{k},q}\right|^2\mathrm{Re}(n_\lambda)\mathrm{Im}\left[\frac{k_z^2/\left(n_\lambda+k_z^2\right)^2}{\left(\omega^2\varepsilon_c - 4\pi i\omega\sigma_c - \frac{c^2k^2}{1+\frac{k_z^2}{n_\lambda}}\right)^2}\right]$$

$$\times\left[k_x^2\sin^2(k_x x_0)\cos^2\left(k_y y_0\right) + k_y^2\cos^2(k_x x_0)\sin^2\left(k_y y_0\right)\right], \tag{33}$$

$$\mathcal{R}_{j,\sigma_{ab}}(\mathbf{r}_0) = \mathcal{A}_J c^2\left|g_{\mathbf{k},q}\right|^2\mathrm{Im}(n_\lambda)\mathrm{Re}\left[\frac{k_z^2/\left(n_\lambda+k_z^2\right)^2}{\left(\omega^2\varepsilon_c - 4\pi i\omega\sigma_c - \frac{c^2k^2}{1+\frac{k_z^2}{n_\lambda}}\right)^2}\right]$$

$$\times\left[k_x^2\sin^2(k_x x_0)\cos^2\left(k_y y_0\right) + k_y^2\cos^2(k_x x_0)\sin^2\left(k_y y_0\right)\right], \tag{34}$$

with

$$\mathcal{A}_J = 4\pi\frac{S_l}{L_x L_y}\frac{2\pi cs}{\Phi_0}\frac{j_j^2}{8\eta_q}.$$

We see that there are two typical spatial patterns corresponding to the c-axis and in-plane responses. The patterns corresponding to σ_c- and j_J- responses have the same symmetry, but somewhat different shapes. A finite in-plane response only appears when the nonuniformity

of the mode along the z direction is taken into account. Typical spatial patterns for c-axis and in-plane response channels are illustrated in Figure A1 for three different modes.

Note that the sum $\mathcal{R}_{\lambda^{-2},a}(\mathbf{r}_0) + \mathcal{R}_{\sigma_{ab},a}(\mathbf{r}_0)$ has a somewhat simpler presentation

$$\mathcal{R}_{\lambda^{-2},a}(\mathbf{r}_0) + \mathcal{R}_{\sigma_{ab},a}(\mathbf{r}_0) = \mathcal{A}_J c^2 \left|g_{\mathbf{k},q}\right|^2 \mathrm{Im}\left[\frac{\frac{k_z^2}{n_\lambda}\left(1+\frac{k_z^2}{n_\lambda}\right)^{-2}}{\left(\omega^2\varepsilon_c - 4\pi i\omega\sigma_c - \frac{c^2k^2}{1+\frac{k_z^2}{n_\lambda}}\right)^2}\right]$$

$$\times\left[k_x^2\sin^2(k_x x_0)\cos^2\left(k_y y_0\right) + k_y^2\cos^2(k_x x_0)\sin^2\left(k_y y_0\right)\right]$$

This analysis reveals that all spatial patterns display maxima/minima at the edges of the mesa, never nodes. Thus, our experimental observations shown in Figs. 1 and 4 demonstrate that a composite mode is activated.

Figures

Figure 1 (Color online only)

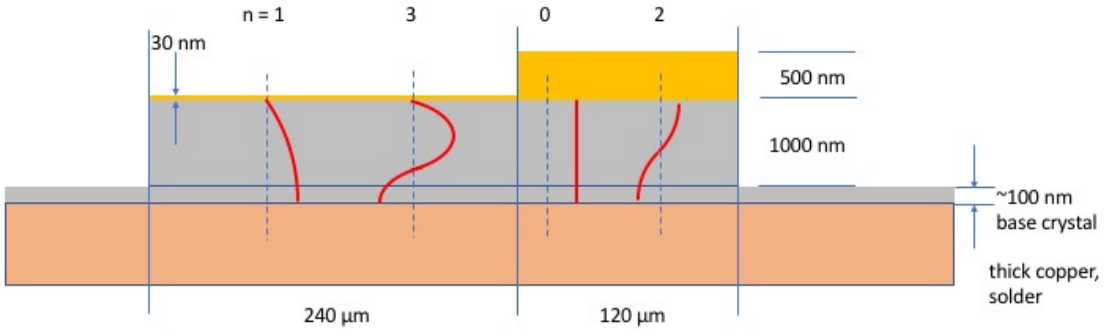

Figure 2 (Two-column figure, Color online only)

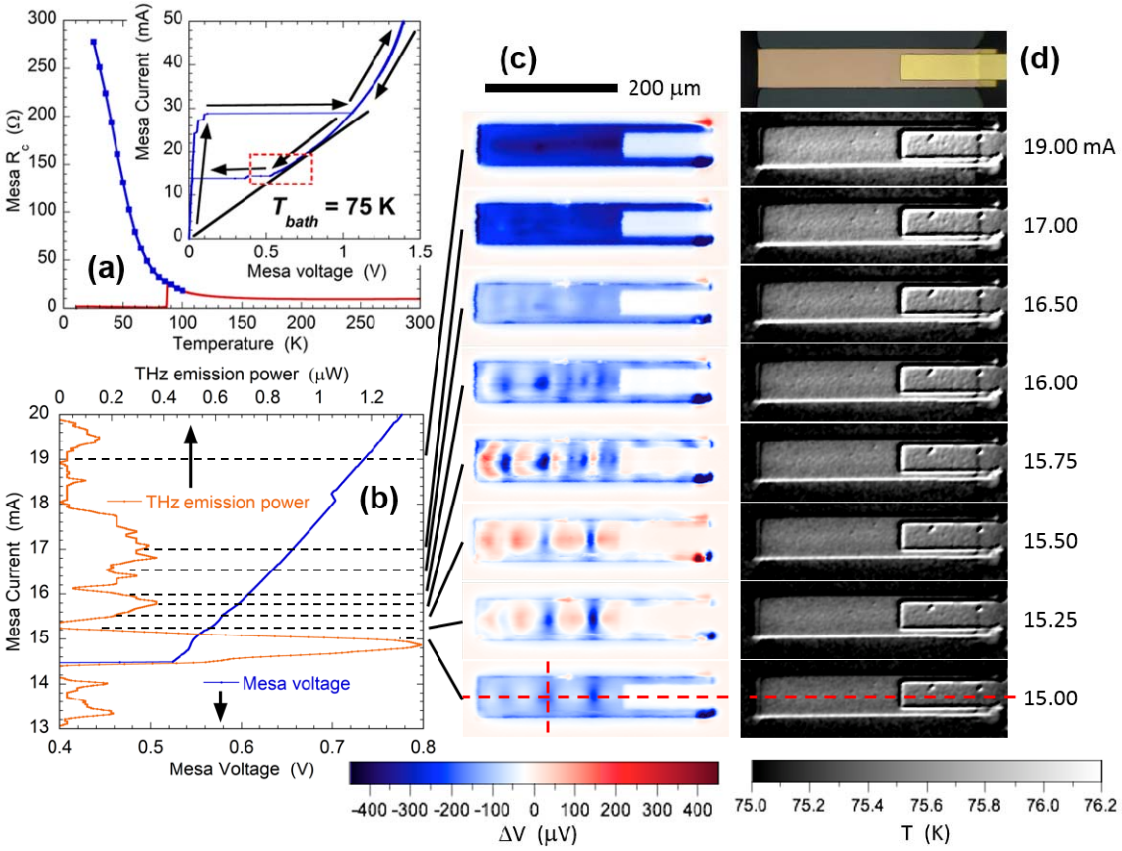

Figure 3 (Color online only)

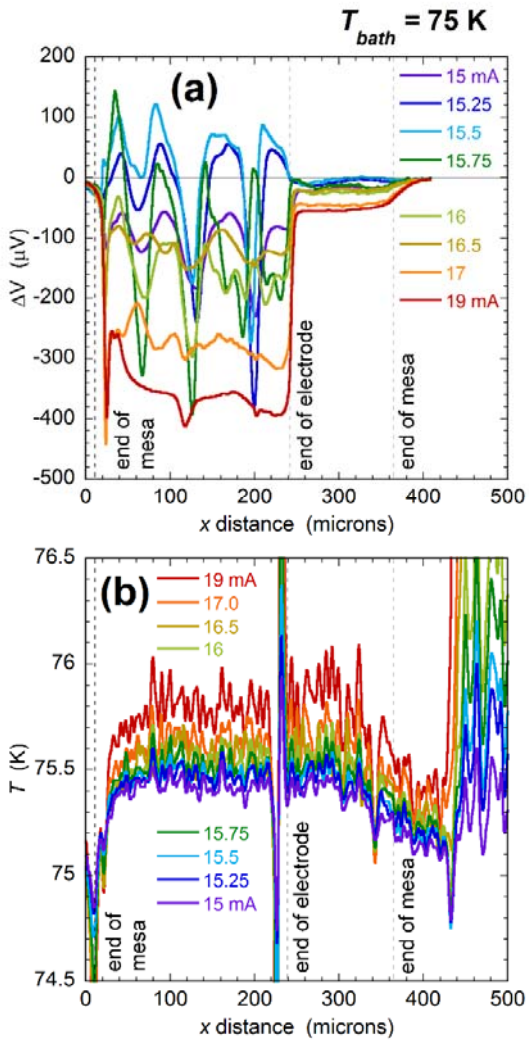

Figure 4 (Color online only)

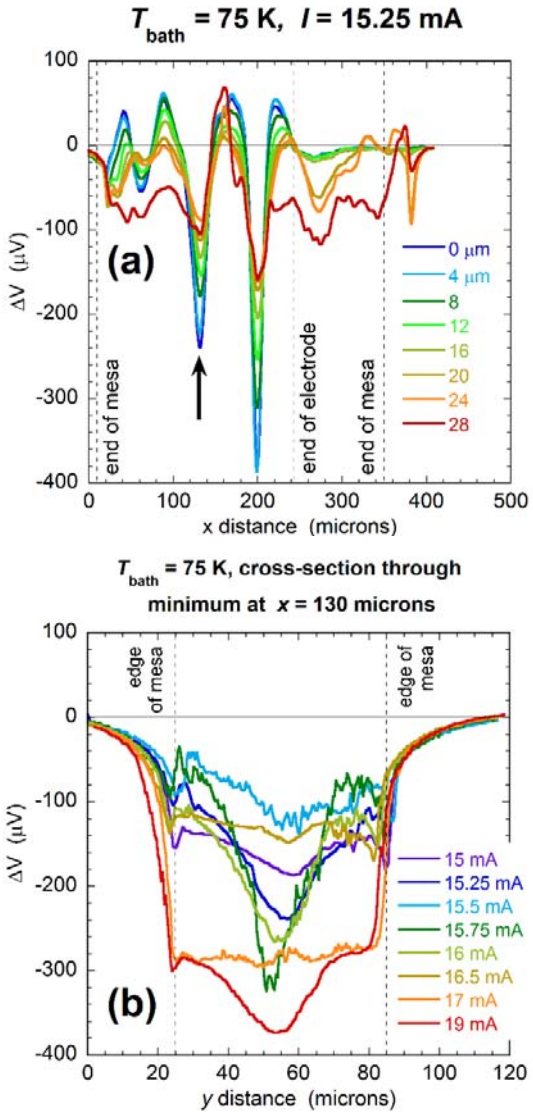

Figure 5 (Color online only)

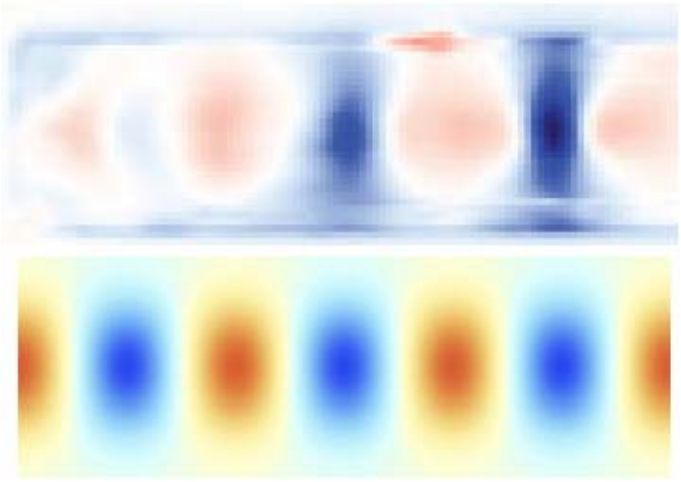

Figure 6 (Color online only)

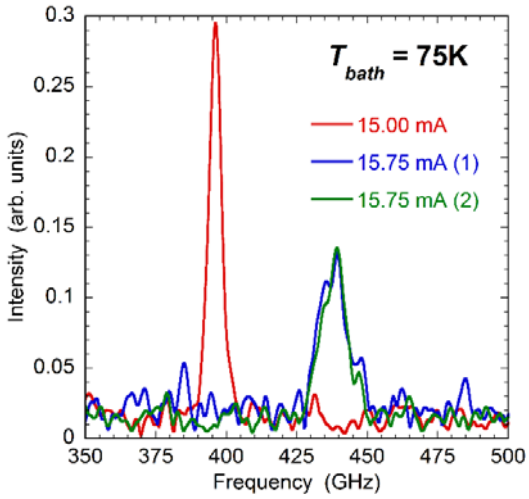

Figure A1 (Two-column figure, Color online only)

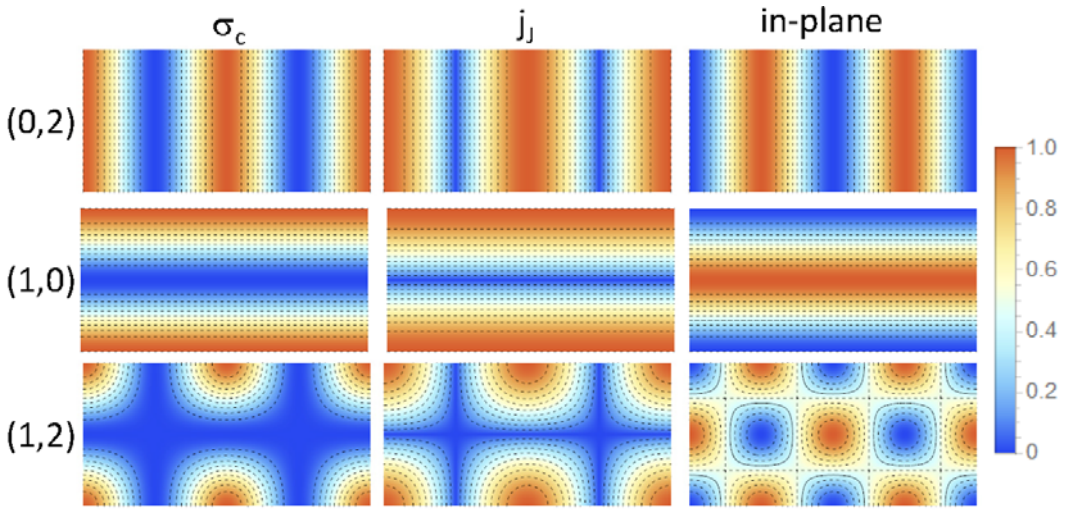

Figure A2 (Two-column figure, Color online only)

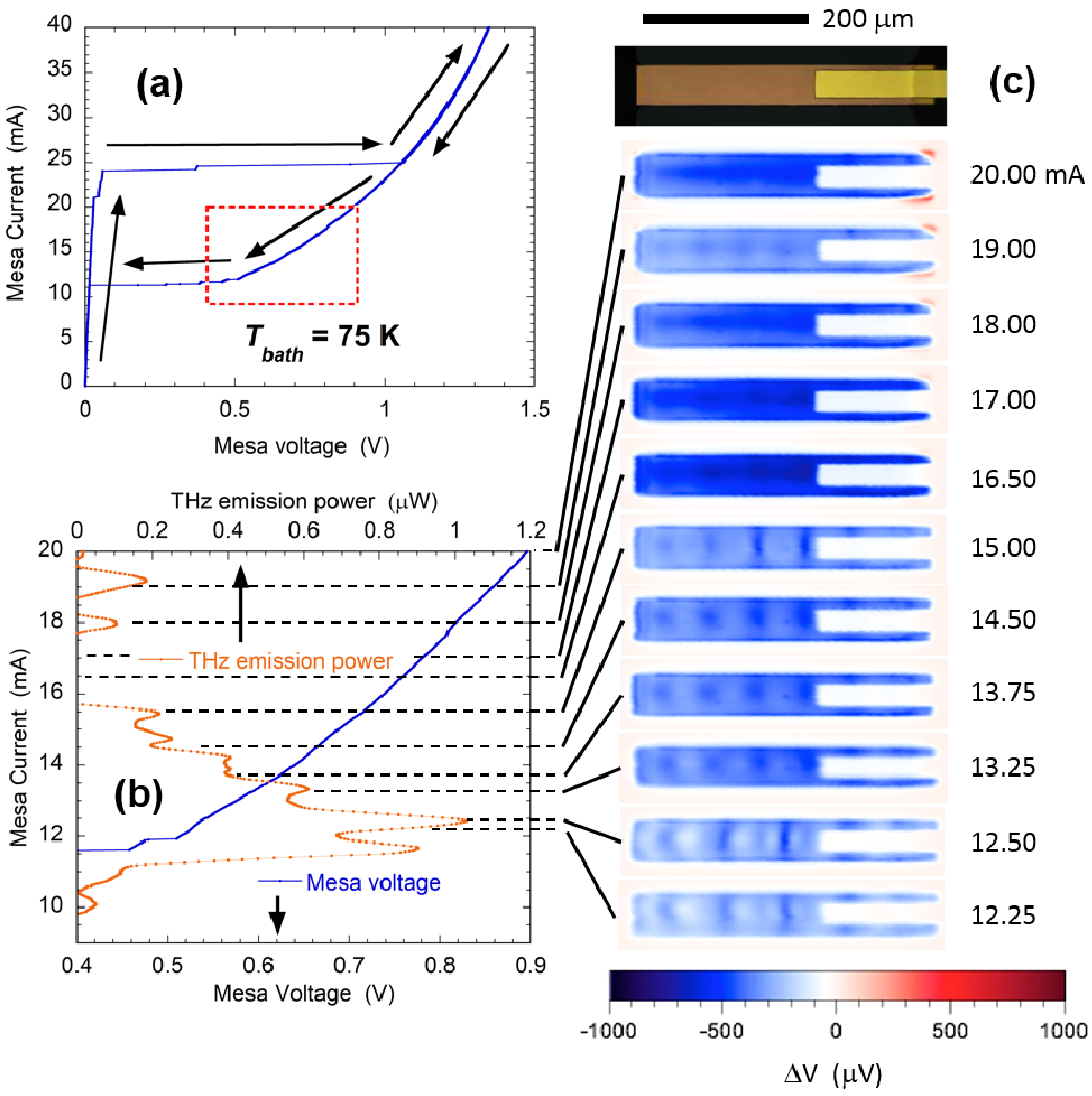

Figure A3 (Two-column figure, Color online only)

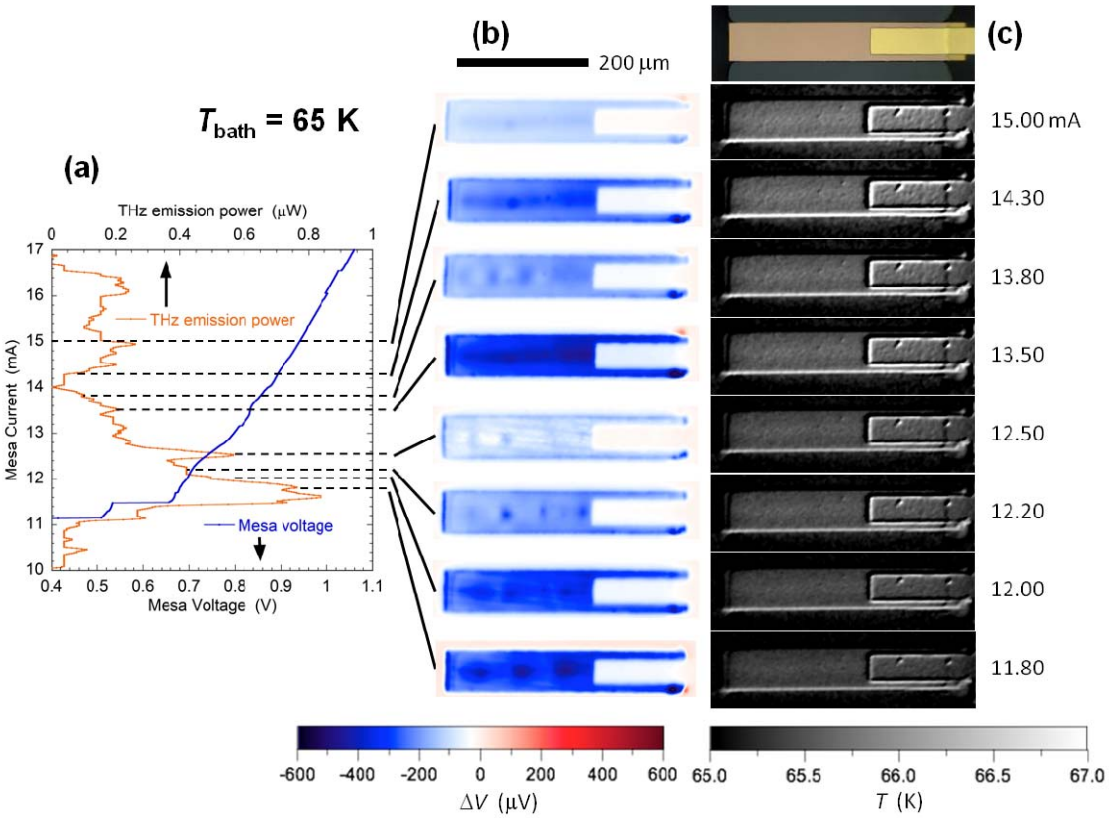

Figure A4 (Color online only)